Microelectronic Engineering 179 (2017) 83–90

Contents lists available at ScienceDirect

Microelectronic Engineering

journal homepage: www.elsevier.com/locate/mee

Research paper

# Frequency-based detection of female *Aedes* mosquito using surface acoustic wave technology: Early prevention of dengue fever

Zaid T. Salim [a,*], U. Hashim [a,*], M.K.Md. Arshad [a], Makram A. Fakhri [a,b,*], Evan T. Salim [c]

[a] Institute of Nano Electronic Engineering, University Malaysia Perlis, 01000 Kangar, Perlis, Malaysia
[b] Laser and Optoelectronic Eng. Dep., University of Technology, 10066 Baghdad, Iraq
[c] Applied Science Dep., University of Technology, 10066 Baghdad, Iraq

ARTICLE INFO

*Article history:*
Received 7 October 2016
Received in revised form 2 April 2017
Accepted 15 April 2017
Available online 20 April 2017

*Keywords:*
Dengue fever
*Aedes* mosquito
Wing beat frequencies
Surface acoustic wave sensor

ABSTRACT

The increasing cases of dengue fever (DF) and dengue hemorrhagic fever (DHF) in the last decade have been reported worldwide. These conditions have led to huge economic loses and health complications. At present, no direct cure for DF and no efficient device to control or detect the *Aedes* mosquitoes that cause DF are available. Therefore, the fabrication of a device will reduce the probability of get infection since it works as a warning system, to exterminate *Aedes* mosquitoes as soon as discovered, and to evacuate the location until it be treated. This paper is the first to report the detection of the female *Aedes* mosquito in human habitations using a surface acoustic wave (SAW) sensor. The feasibility of an acoustic-based device that records differences in signals and noise levels from different mosquito species has been demonstrated in instructing frequency differences to detect female mosquitoes. The SAW sensor response was investigated with simulated and real *Aedes* mosquito signals. Decreased resonant peak amplitude was obtained with different wingbeat frequencies. The $S_{11}$ magnitude was reduced by 0.6 dB and 1.25 dB with female and male *Aedes* mosquitoes, respectively. Furthermore, the SAW sensor exhibited good sensitivity in low sound pressure environments between 40 and 55 dB, making it suitable for use inside an average home.



## 1. Introduction

Dengue fever is one of the most dangerous mosquito-borne diseases that have become a serious health concern [1]. During the 18th and 19th centuries, sailing ships primarily contributed to expanding both the mosquito vector (genus *Aedes*) and the virus responsible for dengue fever worldwide [2]. Mosquitoes completed their life cycles and spread to new areas when a ship called to port through the water stored in ships. The dengue virus can be classified into four serotypes (DEN-1, DEN-2, DEN-3, and DEN-4) and a new surprising, recently discovered serotype (DEN-5) [3]. The symptomatic infections of dengue virus include three categories: undifferentiated fever, dengue fever (DF), and dengue hemorrhagic fever (DHF). Furthermore, DHF is classified into four grades of severity, wherein grades three and four DHF develops into dengue shock syndrome (DSS) [4]. The genus *Aedes* is considered as the main vector for numerous fatal diseases. The most prominent species in this genus are *Aedes aegypte* and *Aedes albopictus* [5]. These species are responsible for transmitting dengue fever, West Nile fever, chikungunya, eastern equine encephalitis, and many other less harmful diseases to humans [6]. The females of this species can transmit all dengue virus serotypes in humans through a bite to have a blood meal and to gain the necessary protein for egg production [7]. Mature *Aedes* mosquito females may spend a lifetime circulating in or around human habitations where they feed and breed [8].

Dengue incidents are increasing worldwide. Previous studies estimated that 50 million dengue infections occur annually, and approximately 2.5 billion people are living in dengue-infested areas [9]. In the last decades, the DF incident has increased dramatically as the geographic presence of *Aedes* mosquitoes expanded to new countries [10]. Current control methods have not stopped the spread of *Aedes* mosquitoes and dengue virus worldwide. Currently no vaccine against dengue virus is licensed. However, a recombinant vaccine (CYD-TVD) has shown efficacy against symptomatic dengue disease [11]. This condition has led to a worldwide resurgence of dengue and has highlighted the urgent need for a novel and sustainable device to control *Aedes* mosquitoes in human habitations.

The measurement of caged individual mosquitoes indicated the technological feasibility of constructing an acoustical device to detect individual mosquitoes. Such a device can distinguish males

* Corresponding authors.
*E-mail addresses:* zaidtareq86@gmail.com (Z.T. Salim), uda@unimap.edu.my (U. Hashim), makram_76@yahoo.com (M.A. Fakhri).

http://dx.doi.org/10.1016/j.mee.2017.04.016
0167-9317/

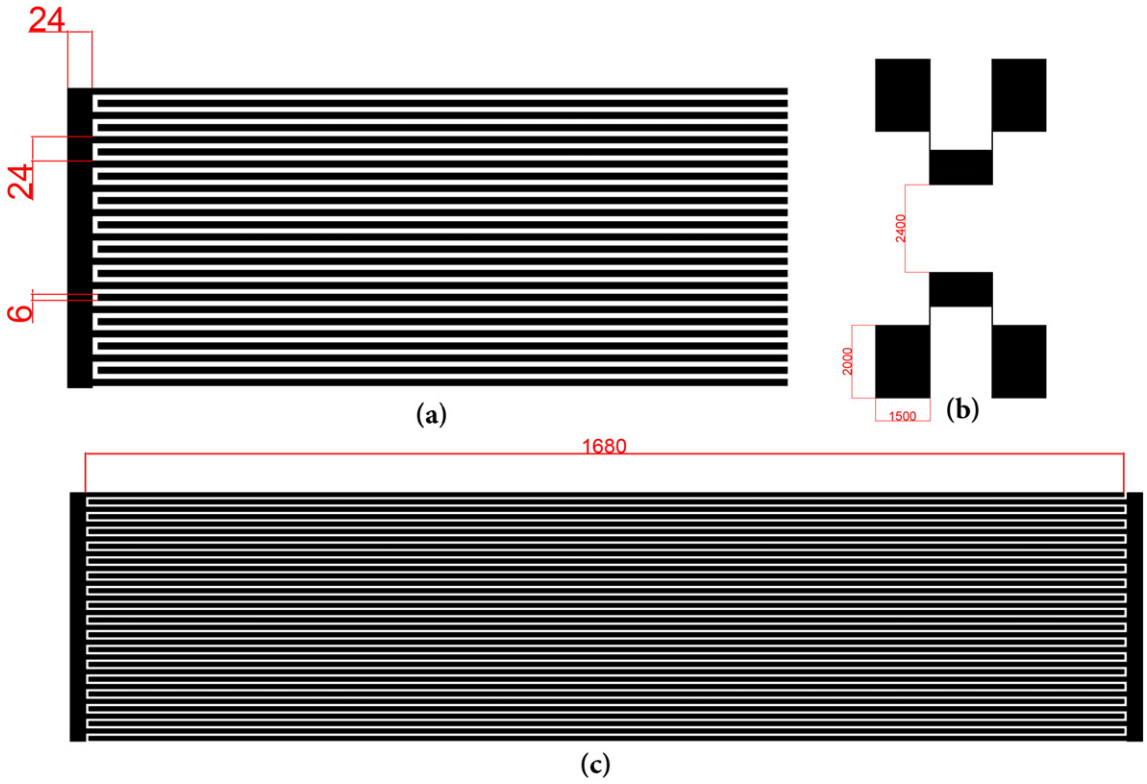


**Fig. 1.** IDT electrodes parameters in microns where; the wavelength, gap between ports and acoustic aperture is highlighted in (a), (b) and (c) respectively.

from females through their wingbeat frequencies. Mankin [12] reported that the wingbeat frequency produced by the flight tone of mosquitoes varied on the basis of genus and gender. Wingbeat frequencies of *Ae. aegypti* and *Ae. albopictus* fall within the range of 400–500 Hz in females and 700–900 Hz in males [12,13].

As sensors, SAW devices takes advantage of the inverse piezoelectric effect in its operation. A SAW will be transmitted and received by the input and output IDTs respectively. Any changes to the SAW characteristics (frequency or amplitude) by external physical or chemical phenomena will be recorded and analyzed [14]. The high sensitivity of SAW devices toward various physical and chemical phenomena is widely known. As sensors, these devices can offer innovative solutions for a wide range of applications [15]. These devices are simple, inherently robust, and competitively priced. Furthermore, they can be passive (no power source) and wireless (can be operated remotely) [16]. A large number of applications have been reported in the literature on SAW devices such as SAW chemical, pressure, and temperature sensors, as well as several other commercial applications [17–21]. In this paper, we report the detection of female *Aedes* mosquitoes in human habitations using a SAW sensor based on the ZnO/IDT/128° YX $LiNbO_3$ structure. The sensor demonstrates good sensitivity toward the changes in frequencies produced by simulated and real mosquito flight tones.

The rest of this paper is organized as follows: Section 2 presents the design and experiment performed to fabricate a two-port layered SAW sensor. Furthermore, it presents the methods and tools

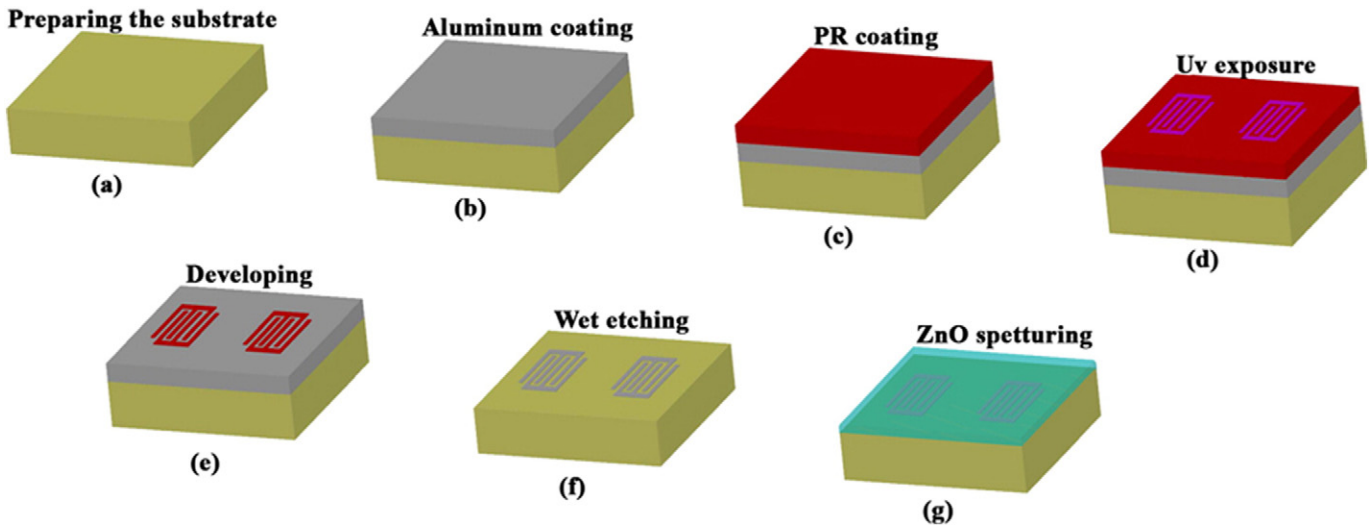


**Fig. 2.** Fabrication schematic of two-port layered SAW device.

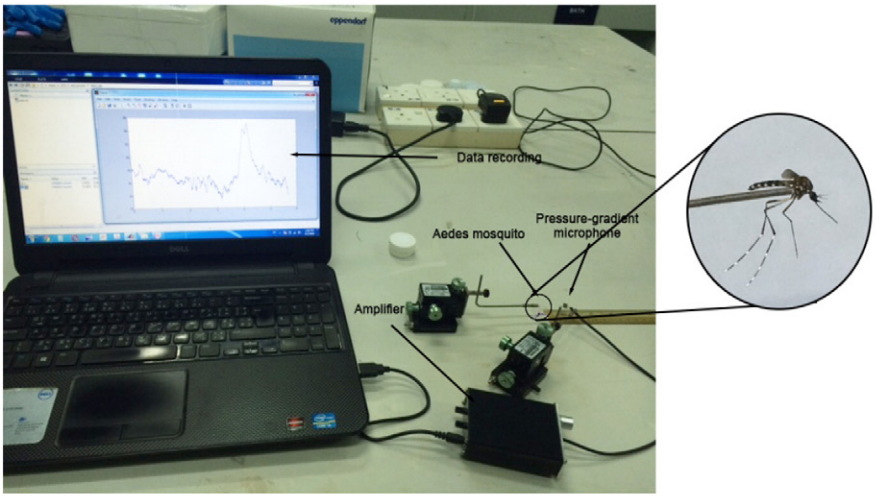


(a)

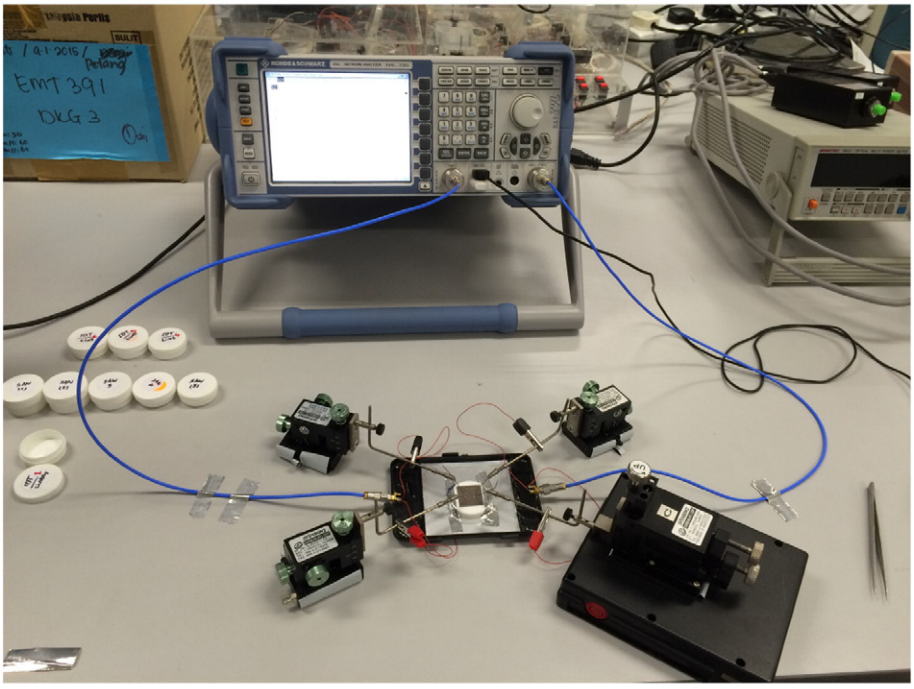

(b)

**Fig. 3.** Setup used to (a) capture the mosquito's wingbeat frequency (b) characterizes the SAW sensors.

used to characterize the SAW sensor. The surface properties, sensitivity, and performance of the SAW sensor are provided in Section 3. Finally, the conclusion is provided, along with a number of directions for future work.

## 2. Design and experiment

The performance of SAW devices is governed by various parameters. A material with high phase velocity, large electromechanical coupling coefficient ($K^2$), and low temperature coefficient of frequency (TCF) is desirable [22]. However, device performance and sensitivity are dramatically affected by the thickness and properties of each layer in the structure of layered SAW devices [23]. A 128° YX cut $LiNbO_3$ substrate was selected for the female *Aedes* mosquito sensors because of its high SAW velocity (3996 m/s) and large electromechanical coupling coefficient (5.5%) [24]. A 1.5 μm thick Zinc oxide (ZnO) layer is deposited on the substrate to maximize the SAW device coupling coefficient [25,26]. By increasing the coupling coefficient, more sufficient SAWs penetrate near the surface, thereby enhancing the sensitivity and performance of the SAW device [27].

The SAW device operation frequency ($f_o$) is governed by the phase velocity ($v_p$) of the piezoelectric substrate and the SAW wavelength ($\lambda$), which results in the following equation [28]:

$$f_0 = v_p/\lambda \tag{1}$$

The SAW wavelength is controlled by the distance between two electrode fingers (periodicity). In this study, the periodicity was fixed to 24 μm, which enabled the device to operate in the VHF range. In the experiment, a two-port delay line structure was utilized in the IDT pattern, and each IDT was fixed with 40 finger pair. The distance between

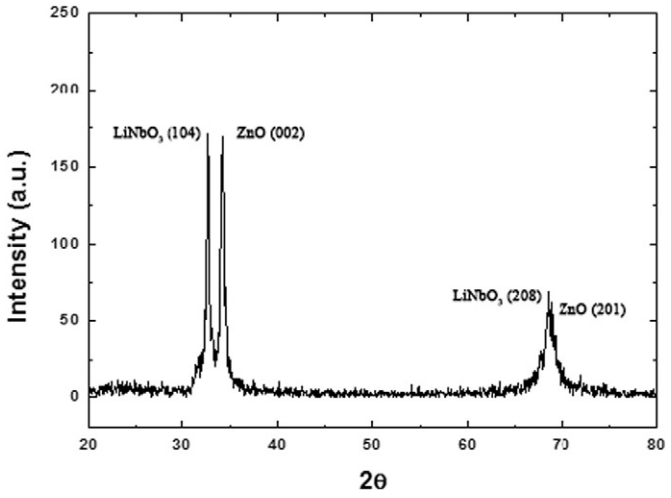


**Fig. 4.** X-ray diffraction results of ZnO nanostructure on $LiNbO_3$.

the ports was set to 100 λ. The acoustic aperture was fixed to 70 λ to avoid losing large diffraction. Fig. 1 shows the IDT pattern used in this study.

A 128° YX $LiNbO_3$ wafer with 0.5 mm thickness and 101.6 mm (4 in.) diameter was used to prepare the SAW device substrate. Using a diamond scriber, the wafer was cut into square-shaped 20 mm samples. To eliminate impurities such as organic materials and dust particles from the substrates, a standard cleaning procedure was conducted. Each sample was immersed in a $H_2O/HCl/H_2O_2$ solution with a ratio of 60:10:10 mL for 5 min at 90 °C, acetone ($CH_3OH$) for 5 min at 60 °C, and methanol ($(CH_3)_2CO$) in the ultrasonic path for 5 min at 60 °C.

Thermal evaporation technique was used for the IDT metallization. BOC Edwards Auto 306 Vacuum Coating System was used to deposit a 200 nm aluminum (99.999% purity) layer on the samples. In this process, aluminum was evaporated under vacuum by maintaining the vacuum chamber pressure below 50 μTorr to prevent any reaction between the aluminum vapor and atmosphere gases. The current was set as 50 mA with a 5.3 nm/s deposition rate.

A positive tone photoresist (PR) from Futures Inc. type PR1-2000A was used after the aluminum deposition process since has a better adhesion to the surface than HMDS. The PR was spin coated at 800 rpm for 10 s, and then at 4000 rpm for 40 s to obtain a film thickness of 1.6–1.8 μm. Samples were then soft baked on a hot plate at 100 °C for 60 s. Soft baking enhanced the adhesion between the PR layer and the sample surface, as well as reduced the solvent concentration in PR, leading to the removal of air bubbles and avoidance of mask contamination with the sticky PR material during lithography. Chromic photomask was used to transfer the IDT pattern presented in Fig. 1 to the samples by using MIDAS UV-Exposure System MDA-400 M. In this process, PR was exposed to UV light with a 365 nm wavelength for 10 s. Each sample received approximately 100 mJ of UV power after the exposure. RD6 developer was used to develop the UV-exposed samples. The developing time and developer concentration are related to the PR layer thickness and the critical dimensions of the pattern. In this work, the developer solution was diluted (15:25) in 15 ml of deionized water and 25 ml of DR6 to control the developing rate more effectively. Samples were immersed in the solution for approximately 60–65 s, and then immersed in deionized water. Thereafter, the samples were inspected for any imperfections in the developing process under a high-power optical microscope. The confirmed samples were then hard baked on a hot plate at 120 °C for 2 min to ensure that the patterned PR layer is stable and firm during the wet etching process.

**Table 1**
Structural properties of ZnO nanostructure on $LiNbO_3$ substrate.

| Properties | Value |
|---|---|
| 2θ | 34.2773 |
| FWHM | 0.3444 |
| c(Å) | 5.2062 |
| D(nm) | 21.053 |
| Strain $\varepsilon_{zz}$ (%) | 0.8999 |

In wet etching, the chemical reaction between the etchant and the etched materials removes the areas unprotected by the PR pattern. Calcium Carbonate ($CaCO_3$) was used for the wet etching. Samples were inspected with a high-power microscope (HPM) to ascertain that high-resolution IDTs were produced.

RF magnetron sputtering was conducted to deposit the zinc oxide film using ZnO target (99.99% purity). Argon (Ar) was used as sputtering gas with a 50 sccm flow rate. The target was placed 50 mm away from the substrate. A pre-sputtering procedure was performed to eliminate any possible target contamination. The RF power was 50 W, and the chamber pressure was fixed at 10 mT. Fig. 2 presents a schematic of the fabrication procedure.

The structural properties of the prepared nanomaterial was investigated using an X-ray diffractometer, (X'Pert Pro MRD PW3040 system) equipped with Cu-Kα radiation of wavelength λ = 0.15418 nm. Morphological properties were characterized using an atomic force microscope (AFM) (SII Sciko Instrument Inc., SPI 3800N Probe). A two-port R&S ZVL Vector Network Analyzer was utilized to analyze the SAW sensor. The sensor response was investigated through simulated mosquito signals ranging from 400 Hz to 900 Hz with an 80 dB sound pressure level (SPL) using MATLAB 2015b. The signals were applied to the SAW sensor through a commercial amplifier. A total number of 6 male and 7 female *Ae. albopictus* mosquitoes were used to investigate the sensor response to the wingbeat frequencies. Measurements were performed in a quiet room during the day. The mosquitoes were narcotized with cold air to ease the tethering and positioning procedures. Then, the mosquitoes were tethered individually to a steel wire using beeswax and mounted 1 cm away from a pressure-gradient microphone (CMP-5247TF-K, CUI Inc.) to measure air particle velocity. Fig. 3 shows the method used to capture the mosquito's wingbeat frequency and the setup used to characterize the SAW sensor.

## 3. Results and discussion

The X-ray diffraction patterns of the prepared zinc oxide nanostructure on 128° YX $LiNbO_3$ are shown in Fig. 4. All of the observed peaks indicated the successfully grown ZnO nanostructure with a wurtzite structure indexed to the hexagonal phase. The film has two different peaks at (002) and (201) diffraction planes. Scherrer equation was used to calculate the crystallite sizes from the X-ray diffraction spectra as follows [29–31]:

$$D = \frac{0.94\,\lambda}{\beta\cos\theta} \tag{2}$$

where the incident X-ray wavelength (λ) equals 1.5406 Å, β is the full width at half maximum, and θ is the diffraction angle in which the peak of a particular orientation occurs.

The lattice constant *c* of the (002) plane was calculated as follows [32–34]:

$$c = \lambda/\sin\theta \tag{3}$$

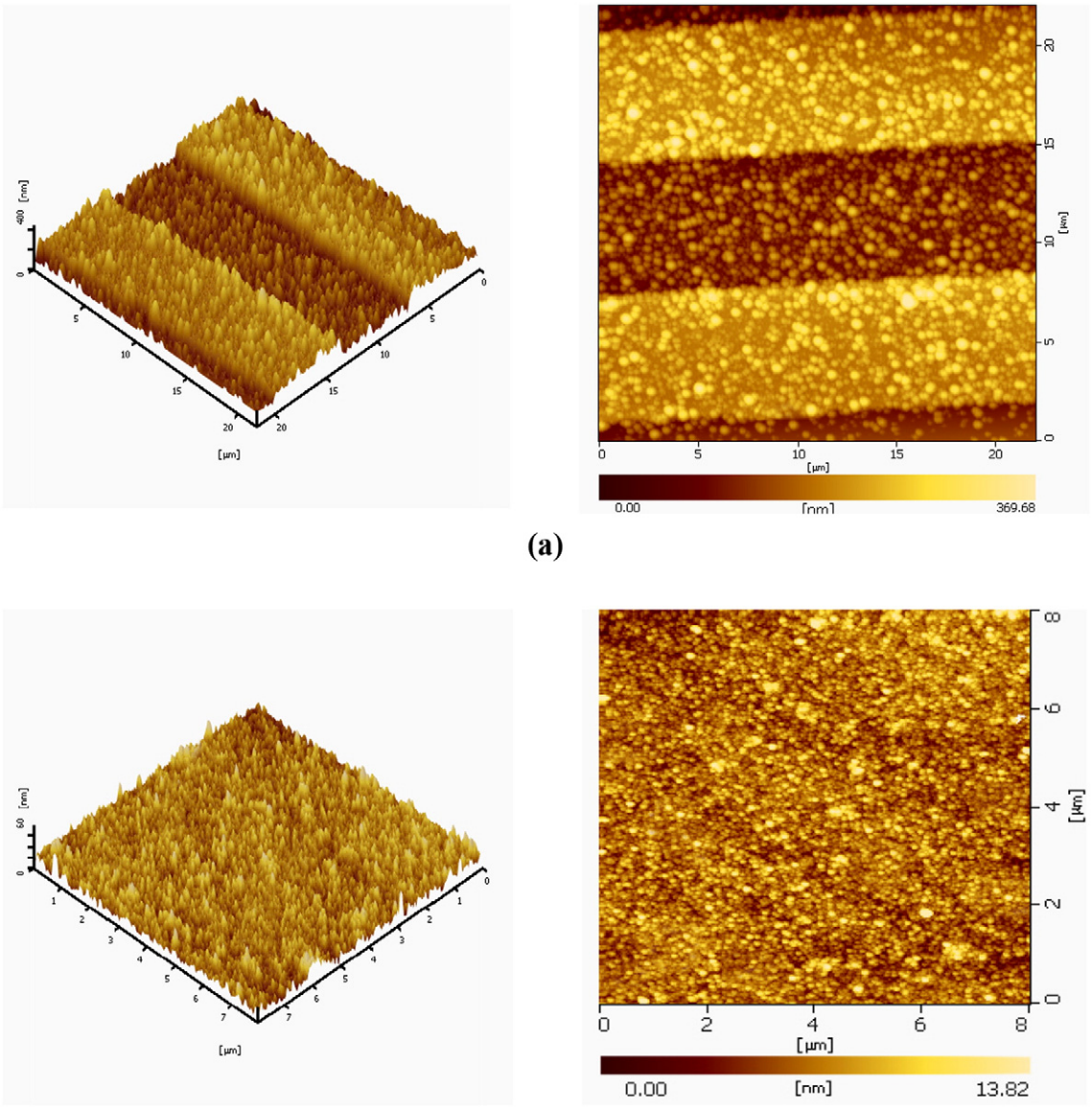


**Fig. 5.** AFM images of sputtered ZnO layer on (a) metalized and (b) non-metalized regions.

The strain ($\varepsilon_{zz}$) of the film notably influences the physical properties because of the lattice mismatch between the ZnO nanostructure and the substrate during the deposition process, which may alter the stress degrees. The strains ($\varepsilon_{zz}$) along the c-axis were calculated using the following formula [35–36]:

$$\varepsilon_{zz}(\%) = \frac{c - c_o}{c_o} \times 100 \quad (4)$$

where the standard lattice constant represented by $c_o$ is 0.5206 nm. Table 1 presents the structural properties of the ZnO nanostructure.

Atomic force microscope characterization was conducted to study the morphological properties of the ZnO nanomaterial in the metalized and non-metalized regions of the structure. Fig. 5(a) shows the measurements over 20 µm × 20 µm on the metalized region. A roughness average (Ra) of 28.97 nm was measured and the root mean square (RMS) value was 36.68 nm. On the non-metalized region, the Ra and RMS were measured as 1.6 nm and 2.1 nm, respectively, as shown in Fig. 5(b). Different growth rates were obtained between the metalized and non-metalized regions, which indicated that the substrate strongly influenced ZnO growth. The smaller Ra and RMS values obtained in the non-metalized region can be attributed to the initial growth of ZnO on a single $LiNbO_3$ crystal unlike the metalized region.

Two surface acoustic waves were utilized. The first port was RF-powered by the network analyzer to create $SAW_1$, whereas the second port was used as the input for the signal produced by the mosquito flight tone to create $SAW_2$. Fig. 6(a) presents the SAW sensor frequency responses at different simulated signals. The frequency response was 158.8 MHz with an $S_{11}$ magnitude of −14.3 dB. The decreased resonance peak amplitude was evident when the wingbeat frequency value increased. The $S_{11}$ magnitude was reduced by 1.27 dB in 900 Hz signal and increased with lower wingbeat frequencies. Higher electric signals were produced by the amplifier as the wingbeat frequency increased. This condition further increased the $SAW_2$ amplitude generated by the second IDT port and the piezoelectric effect. As a result, the interference between $SAW_1$ and $SAW_2$ diminished the $S_{11}$ magnitude. Fig. 6(b) shows the response of the sensor to the wingbeat frequencies produced by female and male *Ae. albopictus* mosquitoes. The standard deviation for male

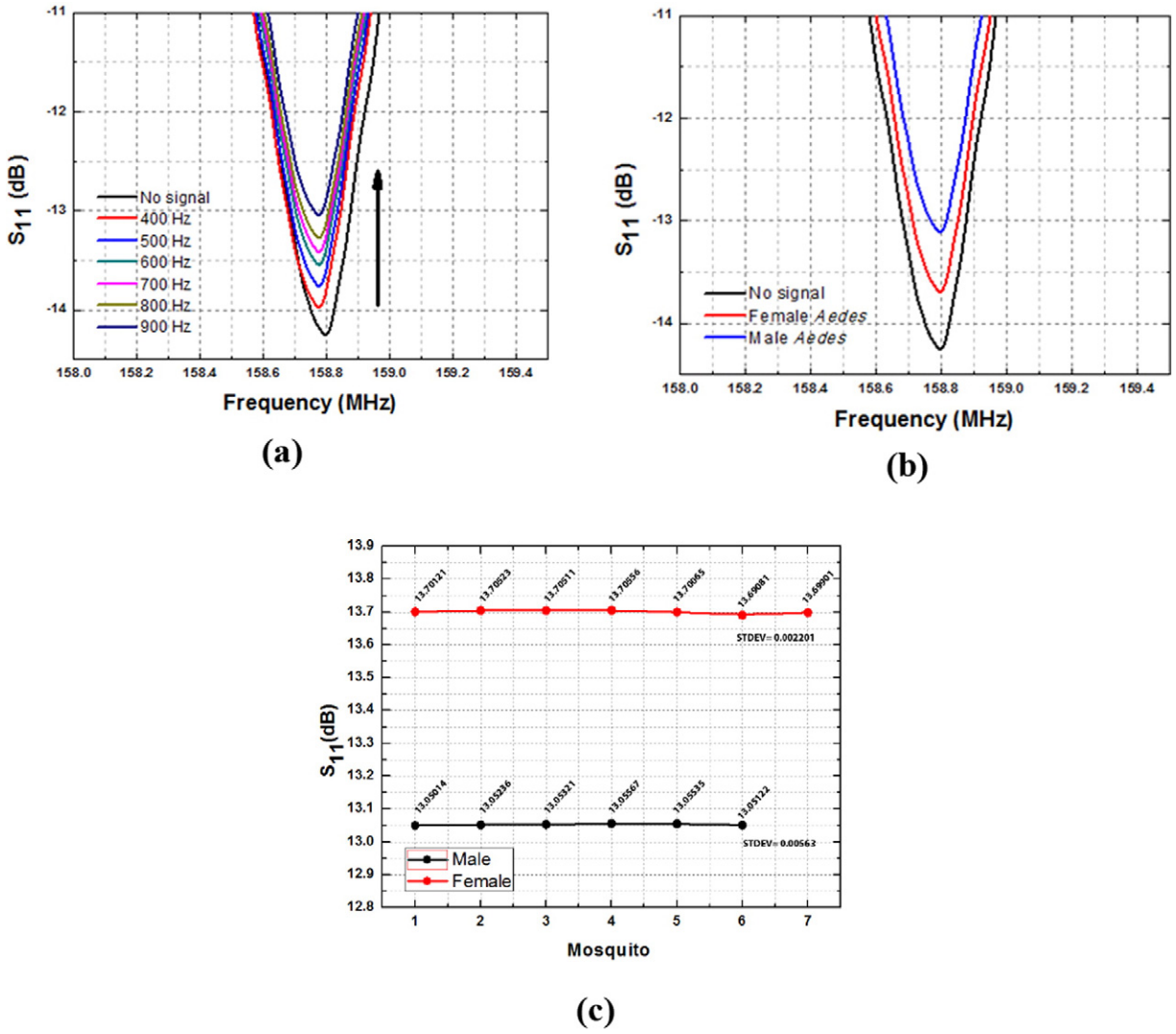


**Fig. 6.** SAW *Aedes* sensor responses with (a) simulated mosquito signals and (b) with real female and male *Aedes albopictus* (c) standard deviation for male and female mosquitoes.

and female mosquitoes is presented in Fig. 6(c). The $S_{11}$ magnitude decreased to −13.7 and −13.05 for the female and the male, respectively. The sound pressure level (SPL) produced by the background noise was measured in different environments. Fig. 7 presents the (SPL) produced by different human habitations.

The sensitivity of the sensor toward female *Aedes* mosquitoes was studied in terms of distance and background noise level. The sensitivity was inversely proportional to the distance. The highest sensitivity at 0.6 dB was obtained between 1 cm and 5 cm where the sound pressure of the mosquito was larger. The sensor detected the female *Aedes* mosquito in 15 cm or the maximum range supported by the microphone. Fig. 8(a) presents the SAW sensor responses to female *Aedes* mosquitoes with varied distances. Fig. 8(b) displays the responses of the sensor toward female *Aedes* mosquitoes with various background noises. The background noise was simulated with MATLAB as the measurements were

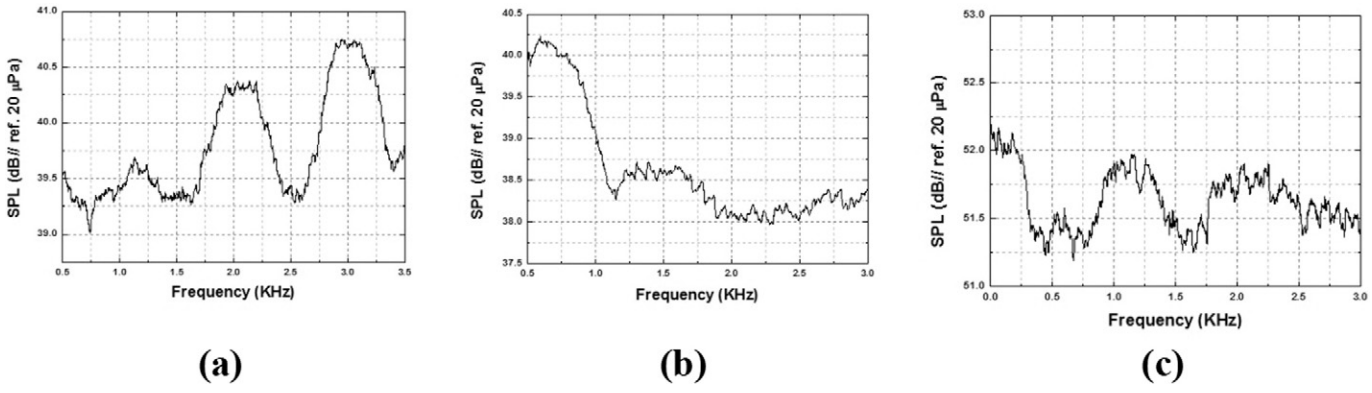


**Fig. 7.** The sound pressure level (SPL) produced by the back ground noise of (a) lab, (b) library and (c) average home.

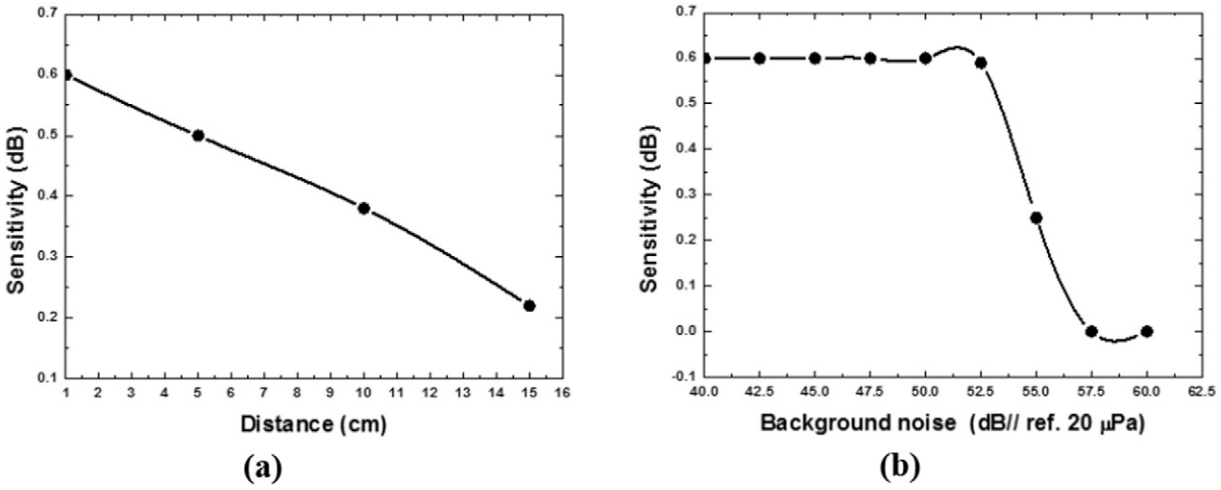


**Fig. 8.** SAW sensor responses to real female *Aedes* mosquito with (a) various distances and (b) background noises.

conducted inside a laboratory with background noise of 40 dB//ref. 20 μPa. The sensor was studied with background noise ranging from 40 dB to 60 dB. The background noise failed to influence sensor sensitivity up to 52.5 dB. However, no response toward the mosquito signal was obtained from the sensor when the background noise increased to 57.5.

## 4. Conclusions

A two-port layered SAW female *Aedes* mosquito sensor based on ZnO/IDT/128° YX $LiNbO_3$ was fabricated. The investigation included the structural and morphological properties of the ZnO thin film. The SAW sensor response to the female *Aedes* mosquito was studied with simulated and real mosquito signals. The SAW sensor shows decreased resonance peak amplitude when the wingbeat frequency value increased and the $S_{11}$ magnitude decreased by 1.27 dB at 900 Hz. The sensor detected the male and female mosquito signals and distinguished one from the other. The highest sensitivity at 0.6 dB was obtained with the female mosquito. The sensor operated with background noise within the range of 40 dB and 55 dB, rendering it suitable for use inside an average home. Sensitivity was influenced by the distance of the mosquito. The maximum range obtained was 15 cm because of the proposed microphone properties. This range can be increased by utilizing a more advance acoustic receiver compared with the one used in this study.

## References

[1] D.J. Gubler, Epidemic dengue/dengue hemorrhagic fever as a public health, social and economic problem in the 21st century, Trends Microbiol. 10 (2) (2002) 100–103.
[2] N.E.A. Murray, M.B. Quam, A. Wilder-Smith, Epidemiology of dengue: past, present and future prospects, Clinical Epidemiology (5) (2013) 299–309.
[3] D. Normile, Surprising new dengue virus throws a spanner in disease control efforts, Science 342 (6157) (2013) 415-415.
[4] S. Ranjit, N. Kissoon, Dengue hemorrhagic fever and shock syndromes, Pediatr. Crit. Care Med. 12 (1) (2011) 90–100.
[5] G. Añez, M. Rios, Dengue in the United States of America: a worsening scenario? Biomed. Res. Int. 2013 (2013).
[6] M.A. Tolle, Mosquito-borne diseases, Curr. Probl. Pediatr. Adolesc. Health Care 39 (4) (2009) 97–140.
[7] T.P. Monath, Dengue: the risk to developed and developing countries, Proc. Natl. Acad. Sci. 91 (7) (1994) 2395–2400.
[8] D.J. Gubler, Dengue and dengue hemorrhagic fever, Clin. Microbiol. Rev. 11 (3) (1998) 480–496.
[9] B.-A.G. Coller, D.E. Clements, Dengue vaccines: progress and challenges, Curr. Opin. Immunol. 23 (3) (2011) 391–398.
[10] S. Bhatt, P.W. Gething, O.J. Brady, J.P. Messina, A.W. Farlow, C.L. Moyes, J.M. Drake, J.S. Brownstein, A.G. Hoen, O. Sankoh, et al., The global distribution and burden of dengue, Nature 496 (7446) (2013) 504–507.
[11] B. Guy, N. Jackson, Dengue vaccine: hypotheses to understand CYD-TDV-induced protection, Nat. Rev. Microbiol. 14 (2016) 45–54.
[12] R. Mankin, Acoustical detection of *Aedes taeniorhynchus* swarms and emergence exoduses in remote salt marshes, J. Am. Mosquito Control Assoc. Mosquito News 10 (2) (1994) 302–308.
[13] B.J. Arthur, K.S. Emr, R.A. Wyttenbach, R.R. Hoy, Mosquito (*Aedes aegypti*) flight tones: Frequency, harmonicity, spherical spreading, and phase relationships, J. Acoust. Soc. Am. 135 (2) (2014) 933–941.
[14] Z.T. Salim, U. Hashim, M. Arshad, M.A. Fakhri, E.T. Salim, Zinc oxide flakes-corolla lobes like nano combined structure for SAW applications, Mater. Res. Bull. 86 (2) (2017) 215–219.
[15] B. Drafts, Acoustic wave technology sensors, IEEE Trans. Microwave Theory Tech. 49 (4) (2001) 795–802.
[16] M. Elhosni, O. Elmazria, S. Petit-Watelot, L. Bouvot, S. Zhgoon, A. Talbi, M. Hehn, K.A. Aissa, S. Hage-Ali, D. Lacour, et al., Magnetic field SAW sensors based on magnetostrictive-piezoelectric layered structures: FEM modeling and experimental validation, Sensors Actuators A Phys. 240 (2016) 41–49.
[17] G. Borrero, J. Bravo, S. Mora, S. Velásquez, F. Segura-Quijano, Design and fabrication of SAW pressure, temperature and impedance sensors using novel multiphysics simulation models, Sensors Actuators A Phys. 203 (2013) 204–214.
[18] W. Li, P. Dhagat, A. Jander, Surface acoustic wave magnetic sensor using galfenol thin film, IEEE Trans. Magn. 48 (11) (2012) 4100–4102.
[19] A. Flewitt, J. Luo, Y.Q. Fu, L. Garcia-Gancedo, X. Du, J. Lu, X. Zhao, E. Iborra, M. Ramos, W. Milne, ZnO based SAW and FBAR devices for bio-sensing applications, J. Non-Newtonian Fluid Mech. 222 (2015) 209–216.
[20] C.-L. Wei, Y.-C. Chen, C.-C. Cheng, K.-S. Kao, D.-L. Cheng, P.-S. Cheng, Highly sensitive ultraviolet detector using a ZnO/Si layered SAW oscillator, Thin Solid Films 518 (11) (2010) 3059–3062.
[21] W. Xuan, M. He, N. Meng, X. He, W. Wang, J. Chen, T. Shi, T. Hasan, Z. Xu, Y. Xu, et al., Fast response and high sensitivity ZnO/glass surface acoustic wave humidity sensors using graphene oxide sensing layer, Sci. Report. 4 (2013) 7206-7206.
[22] S. Maouhoub, Y. Aoura, A. Mir, FEM simulation of Rayleigh waves for SAW devices based on ZnO/AlN/Si, Microelectron. Eng. 136 (2015) 22–25.
[23] O. Legrani, O. Elmazria, S. Zhgoon, P. Pigeat, A. Bartasyte, Packageless AlN/ZnO/Si structure for SAW devices applications, IEEE Sensors J. 13 (2) (2013) 487–491.
[24] H. Oh, K. Lee, K. Eun, S.-H. Choa, S.S. Yang, Development of a high-sensitivity strain measurement system based on a SH SAW sensor, J. Micromech. Microeng. 22 (2) (2012) 025002.
[25] K. Nakamura, T. Hanaoka, Propagation characteristics of surface acoustic waves in ZnO/LiNbO3 structures, Jpn. J. Appl. Phys. 32 (5S) (1993) 2333.
[26] Z.T. Salim, U. Hashim, M. Arshad, M.A. Fakhri, Simulation, Fabrication and Validation of Surface Acoustic Wave Layered Sensor Based on ZnO/IDT/128° YXLiNbO$_3$, Int. J. Appl. Eng. Res. 11 (15) (2016) 8785–8790.
[27] D.A. Powell, K. Kalantar-zadeh, W. Wlodarski, Numerical calculation of SAW sensitivity: Application to ZnO/LiTaO 3 transducers, Sensors Actuators A Phys. 115 (2) (2004) 456–461.
[28] V.B. Raj, A. Nimal, Y. Parmar, M. Sharma, V. Gupta, Investigations on the origin of mass and elastic loading in the time varying distinct response of ZnO SAW ammonia sensor, Sensors Actuators B Chem. 166 (2012) 576–585.
[29] M.A. Fakhri, Y. Al-Douri, U. Hashim, E.T. Salim, Optical investigations of photonics lithium niobate, Sol. Energy 120 (2015) 381–388.
[30] M.A. Fakhri, Y. Al-Douri, U. Hashim, E.T. Salim, Deo Prakash, K.D. Verma, Optical investigation of nanophotonic lithium niobate-based optical waveguide, Appl. Phys. B Lasers Opt. 121 (2015) 107–116.
[31] E.T. Salem, M.A. Fakhri, H. Hassan, Metal oxide nanoparticles suspension for optoelectronic device fabrication, Int. J. Nanoelectronics and Materials 6 (2013) 121–128.
[32] E.T. Sslim, M.S. Al Wazny, M.A. Fakhri, Glancing Angle Reactive Pulsed Laser Deposition (GRPLD) for $Bi_2O_3$/Si Hetrostructure, Mod. Phys. Lett. B 27 (16) (2013) 1350122 (7 pages).

[33] Makram A. Fakhri, Y. Al-Douri, U. Hashim, Evan T. Salim, XRD analysis and morphological studies of spin coated $LiNbO_3$ nano photonic crystal prepared for optical waveguide application, Adv. Mater. Res. 1133 (2016) 457-46.
[34] M. Abdul Muhsien, E.T. Salem, I.R. Agool, H.H. Hamdan, Gas sensing of Au/n-$SnO_2$/p-PSi/c-Si heterojunction devices prepared by rapid thermal oxidation, Appl. Nanosci. 4 (2014) 719–732.
[35] A. Kadhim, Evan T. Salim, S.M. Fayadh, A.A. Al-Amiery, A. Amir, H. Kadhum, A. BakarMohamad, Effect of multipath laser shock processing on microhardness, surface roughness, and wear resistance of 2024-T3 Al alloy, Sci. World J. 2014 (2014), 490951.
[36] Evan T. Salem, Optoelectronic properties of $Fe_2O_3$/Si heterojunction prepared by rapid thermal oxidation method, Indian Journal of Physics 87 (2013) 349–353.